Metals and Materials International (2021) 27:3409–3416
https://doi.org/10.1007/s12540-021-00969-w

# Rapid Consolidation of WC-$ZrSiO_4$ Hard Materials by Spark Plasma Sintering: Microstructure, Densification, and Mechanical Properties

**Jeong-Han Lee[1,2] · Ik-Hyun Oh[1] · Ju-Hun Kim[1,2] · Sung-Kil Hong[2] · Hyun-Kuk Park[1]**

Received: 7 October 2020 / Accepted: 7 January 2021 / Published online: 7 July 2021


**Abstract**
Densely consolidated WC-based hard materials with 5–20 vol% $ZrSiO_4$ was fabricated by spark plasma sintering at 1400 ℃ at a constant heating rate of 70 ℃/min$^{-1}$. To achieve mechanical alloying of WC-$ZrSiO_4$, planetary ball milling was carried out for 12 h, during which the brittle-brittle components (WC-$ZrSiO_4$) became fragmented and their particles became refined. It was observed that certain, specific, non-isothermal sintering kinetics, such as apparent activation energy, sintering exponents, and densification strain, affected the densification behavior. The evolution of phase structure from powder to compact was found to be related the lattice distortion and micro-strain in the basal planes of WC. By examining the mechanical properties of the samples, it was that the added zircon content leads to enhanced fracture toughness (12.9 MPa m$^{1/2}$) owing to the presence of WC-$ZrSiO_4$ in the cemented carbide. In fact, the microcrack propagation of the fracture passed through zircon from a transgranular to a ductile component (fcc) where the crack tips could be absorbed.

**Keywords** Cemented carbide · Zircon · Mechanical alloying · Spark plasma sintering · Sintering kinetics

## 1 Introduction

Hard materials, such as cemented carbide, cermets, and ceramic composites, have been widely used in cutting tools that are employed in machining various difficult-to-cut materials [1, 2]. In particular, WC-Co cemented carbides are the most popular because of their high stiffness, hardness, wear resistance, and temperature stability [3, 4]. However, even when hard materials are used, the cutting tools are vulnerable to wear and tear, which softens the tools and reduces their lifespan, during the high speed and high temperature cutting process [5].

When maching conductive materials (workpiece) that heat up rapidly due to the discharge of electrictiy, the Co phase on the surface of the cemented carbide dissolves. This leads to the formation of a molten layer, which in turn causes the softening of the cutting tool [6, 7]. Furthermore, surface corrosion may occur owing to the ionization of Co caused by the cutting oil or grinding fluid used during wet working. This causes WC particles at interface of WC/Co to fall off, which eventually leads to a reduction in tool life [1, 8].

To overcome the electrochemical instability in WC-Co, the metallic binders can be replaced by refractory materials, such as zircon ($ZrSiO_4$), because they possess excellent thermophysical properties like low thermal conductivity, good corrosion resistance, and high chemical inertness [9–11]. Moreover, zircon is an abundant raw material that is cheaper than cobalt. The inertness of zircon also makes it more environmentally friendly than cobalt, which can cause enviromental contamination, when used in cemented carbide tools [12, 13].

As the composite comprise tungsten carbide, zircon should be sintered and should retain a homogeneous distribution to ensure that the composite has excellent bending and toughness properties at high temperatures [14]. In other words, the thermal dissociation of zircon due to cooling can cause rapid variations in its volume and crystal structure (tetragonal to monoclinic), which will lead to the deterioration of the mechanical properties of the component [4, 15]. Sintering compatibility is enhanced by a planetary ball milling process that mechanically alloys the composite by forming brittle-brittle components

✉ Hyun-Kuk Park
hk-park@kitech.re.kr

[1] EV&Components Materials Group, Korea Institute of Industrial Technology (KITECH), 61012 Gwangju, Republic of Korea

[2] Materials Science and Engineering, Chonnam National University, Gwangju 61186, Republic of Korea

($WC\text{-}ZrSiO_4$) [16]. In addition, several studies have reported that dissociation of zircon can be prevented by ensuring full densification at low temperatures through a rapid heating rate accelerated by the joule and pulse current effects of spark plasma sintering (SPS) [17–19]. However, only few studies have reported the effect of the sintering kinetics and structural evolution of $WC\text{-}ZrSiO_4$ hard materials on their mechanical properties. In particular, it is worth discussing whether these novel composites possess the mechanical properties required for cutting tools applied at high speeds and temperatures.

Thus, the aim of this study was to obtain fully dense $WC\text{-}ZrSiO_4$ hard materials from different powders varing in particle size and physical properties, and to observe how they prevent the dissociation of zircon due to the rapid consolidation of compacts in SPS, which was preceded by the planetary ball milling process wherein the powders were mechanically alloyed.

## 2 Experimental Procedure

Tungsten carbide (W: 94.0 wt% and C: 6.0 wt%, ≤ 0.5 µm, TaeguTec Ltd.) and zircon sand ($ZrO_2$: 67.04 wt%, $SiO_2$: 29.01 wt%, other oxides: 3.95 wt%, TMG Ltd.) powders were used as the starting materials. These powders were mechanically alloyed by a planetary ball mill (Pulverisette 5, FRITSCH Ltd.) in stainless steel vials with tungsten carbide balls, under a ball-to-powder ratio of 15:1. They were milled for 12 h at 300 RPM in ethanol media (4 wt%). The average particle sizes of the powders were determined by particle size analysis to find D (0.5) (Mastersizer 3000, Malvern Panalytical Ltd.). Where, D is diameter of particle and D (0.5) means the average values. The particle size of WC and $ZrSiO_4$ were 0.84 and 132.62 µm, respectively. After milling, the particle size significantly decreased compared to the starting powders. The particle sizes ranged from 1.69 µm for 20 vol% zircon to 1.40 µm for 5 vol% zircon.

Subsequently, SPS was applied at 1400℃ for 20 min under a pressure of 60 MPa. The influence of sintering kinetics on consolidation behavior was investigated through several routes: (1) macroscopic shrinkage strain (ε); (2) sintering exponent (m); (3) strain rate (dε/dT), and apparent activation energy (Q); and (4) variation of porosity and relative density. The sintering kinetics wae measured by suitable equations or mechanisms.

First, the macro-shrinkage strain and sintering exponents were calculated (Eq. 1) using the dimensional change in shrinkage displacement [20] measured by the SPS instruments.

$$\varepsilon^{\mathrm{m}} = \left(\frac{\Delta L}{L_0}\right)^m = -\left(\frac{X}{2D}\right)^2, \rho_S = \rho_G / \left(1 - \frac{\Delta L}{L_0}\right)^3 \quad (1)$$

In Eq. (1), ΔL is the change in shrinkage displacement, $L_0$ is the original length of the green body, $\rho_S$ is the sintered relative density, $\rho_G$ is the density of the green body, and (X/2D) is the neck-to-particle diameter ratio of the sintered particles.

The apparent activation energy was calculated from strain rate using Dorn's method [21], and the process is described by Eq. (2).

$$\ln(T\varepsilon^m) = \ln(K_0 t) - \frac{Q}{RT}, Q = \frac{RT_1T_2}{T_1 - T_2} ln\left(\frac{v_1}{v_2}\right) \quad (2)$$

where, K is the temperature-dependent sintering constant, T is the hold temperature, t is the isothermal holding time, R is the gas constant ($8.314\,J{\cdot}mol^{-1}{\cdot}K^{-1}$), and $v$ is the sintering rate ($1{\cdot}s^{-1}$) at the applied temperature.

The porosity fraction was calculated using Eq. (3).

$$\mathrm{P}_{\mathrm{porosity}}(\%) = 1 - \rho, \rho = (1 - \varepsilon)^3 p_f \quad (3)$$

where $\rho$ is the instantaneous density and $\rho_f$ is the final density expressed as a fraction of the theoretical density [22].

The structural evolution was analyzed by X-ray diffraction (XRD) using CuKα radiation (wavelength, λ = 0.154 nm). The grain size and internal strain of the $WC\text{-}ZrSiO_4$ hard materials were evaluated by Stokes and Wilson's formula (Eq. 4) [23] using information from the XRD patterns.

$$b = b_d + b_e = k\lambda/(dcos\theta) + 4\varepsilon tan\theta \quad (4)$$

In Eq. (4), b is the full-width at half-maximum (FWHM) of the mechanical correction value of the diffraction peak, and $b_d$ and $b_e$ are the measured values of the decrease in internal stress and FWHM, respectively. $k$ is the Scherr constant 0.9, $\lambda$ is the X-ray radiation wavelength, $\theta$ is Bragg's angle, and $d$ and $\varepsilon$ are measurements of the grain size and the internal strain, respectively.

The hardness ($kg\,mm^{-2}$) and fracture toughness ($MPa\,m^{1/2}$) were determined through indentation cracking with a load of 20 kg f (Vickers pyramid number, HV 20) applied for 15 s. Additionally, the numerical value of the fracture toughness ($K_{IC}$) obtained from the crack propagation lengths in the four directions of the indentations were used to determine the cracking resistance, which was calculated by the Antis formula (Eq. 5) [24].

$$K_{IC} = 0.016\left(\frac{E}{H}\right)^{1/2} P/C^{3/2} \quad (5)$$

where E is the elastic modulus (WC: 696 GPa, $ZrSiO_4$: 255 GPa), H is the hardness, P is the applied load, and C is the length of crack propagation.

## 3 Results and Discussion

Figure 1 displays the WC-20 vol% $ZrSiO_4$ powder as the representative mechanical alloying product in field emission scanning electronic microscopy (FE-SEM) images. After the milling process, individual powders both WC and $ZrSiO_4$ were flattened and fractured to form soft agglomerates, i.e., (a) WC-WC and (b) $ZrSiO_4$-$ZrSiO_4$, with irregular morphologies. During consolidation, these agglomerated particles are intergrated into larger aggregates with pore boundaries, and these particles easily densified through several available diffusion routes [25]. Conversely, (c) the brittle-brittle components [26] composed of WC-$ZrSiO_4$ was the result of the fragmented harder component (WC) itself in the softer component ($ZrSiO_4$). These components are not mechanically alloyed composites, but they have metastable bonds due to interparticle necking [27], which may induce plastic deformations or micro-strain in tungsten carbide during the diffusion process [26, 27].

Figure 2 shows the variation in the sintering temperature and the shrinkage displacement profile for WC-$ZrSiO_4$ hard materials with varying zircon content. All the WC-$ZrSiO_4$ compacts had three inflection points in terms of shrinkage displacement. The applied sintering temperatures were divided into stages I (620–720 °C), II (720–1020 °C), and III (1020–1400 °C). Stage I was stable at temperatures above 600 °C with a pulse ratio that was applied for infrared pyrometer detection, and only 2%–3% densification with slight shrinkage from particle-to-particle contact was achieved from the starting green body. During stage II, the material rapidly shrunk as the active mechanism continued and until densely consolidated compacts containing mass transport, such as neck formation, removal of open pores, densification of volume, grain boundaries, and lattice diffusion, were formed [28]. During stage III, the final densification took place where the removal of closed pores by diffusion, plastic deformation, and grain growth of WC could be observed. In fact, Fig. 3 illustrates the variation in porosity and relative density for the WC-$ZrSiO_4$ compacts. The WC-$ZrSiO_4$ hard materials were almost completely consolidated, with a relative density greater than 98.0%. In particular, it is interesting to note that the highest density 15 vol% zircon compact had the highest relative density 99.3%, followed in a descending order by, 5 vol% zircon 99.0%, 10 vol% zircon,

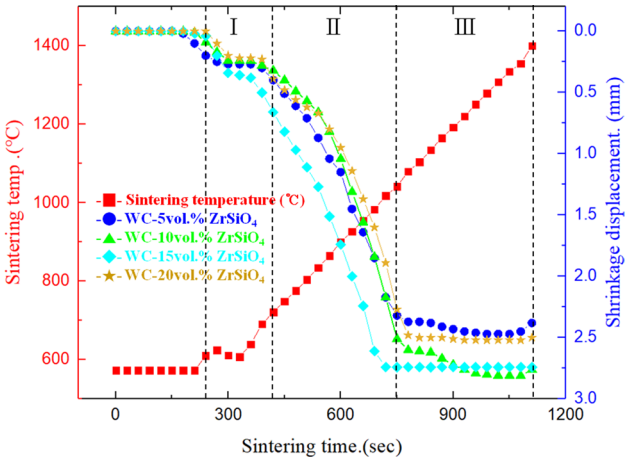


**Fig. 2** Schematic representation of the temperature and shrinkage displacement profile during SPS process

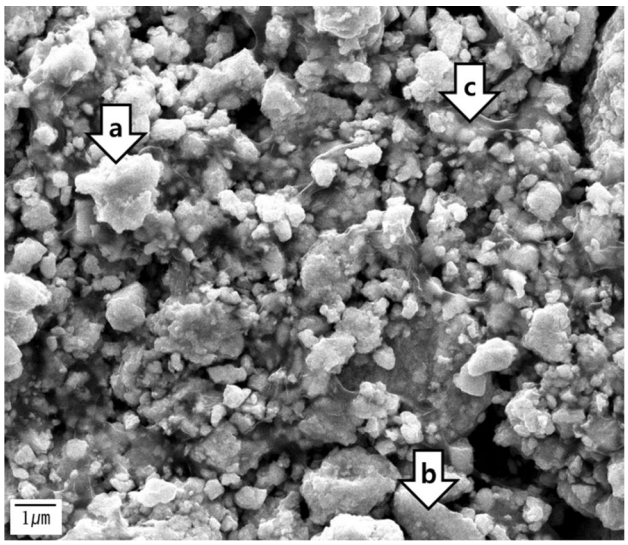


**Fig. 1** Microstructure of WC-$ZrSiO_4$ powder by planetary ball milling process for 12 h: **a** WC, **b** $ZrSiO_4$, and **c** WC-$ZrSiO_4$ component (brittle-brittle)

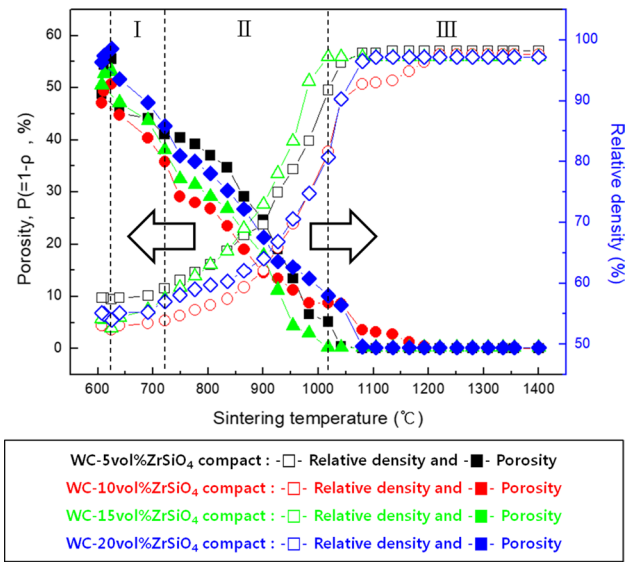


**Fig. 3** Porosity and relative density of WC-$ZrSiO_4$ hard materials

98.5%, and 20 vol% zircon. During stage II, the WC-15 vol% $ZrSiO_4$ reached the densification stage relatively early due to a rapid increase in its relative density. Furthermore, it was implied that the removal of isolated pores occurred durign the final densification [29], which was indicated by the termination of diffusion at the grain boundaries at a relatively low sintering temperature. It was inferred that the brittle-brittle component bonds of the starting powders resulted in an increased contact area for interparticle neck growth and densification [27, 30]. These brittle-brittle components were presumed to be extremely well formed at 15 vol% zircon and was chosen as the threshold content, whereas at 20 vol% zircon it became inefficient for densification because of the removal of isolated pores in the presence of a zircon rich-phase that precipitates at the grain boundaries [31].

The sintering exponents according to the contents of zircon were calculated using Eq. (1), which can also be expressed as a logarithmic function.

$$ln(\varepsilon) = \frac{1}{m} ln\left(\frac{K}{T}\right) + \frac{1}{m} ln(t) \tag{6}$$

Therefore, the sintering exponents can be evaluated as the slope of the shrinkage strain illustrated in Fig. 4. According to the variation of relative density shown in Figs. 3 and 15 vol% zircon, which was considered to be completely densified by the high shrinkage strain, had the least sintering exponent (m = 1.86).

Figure 5 shows apparent activation energy according to strain rate as a function of sintering temperature. In addition, Table 1 displays the apparent activation energies of the three sintering stages, which calculated by Eq. (2). Stage I, low activation energy; this could be due to the

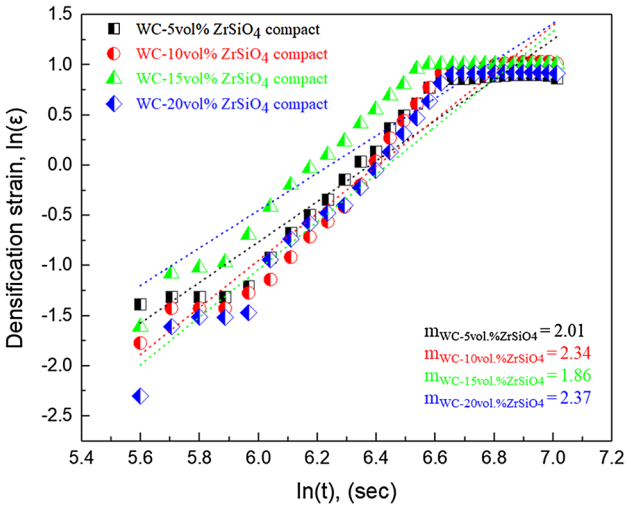


**Fig. 4** Densification strain during SPS process (sintering time) corresponding sintering exponent of WC-$ZrSiO_4$ hard materials

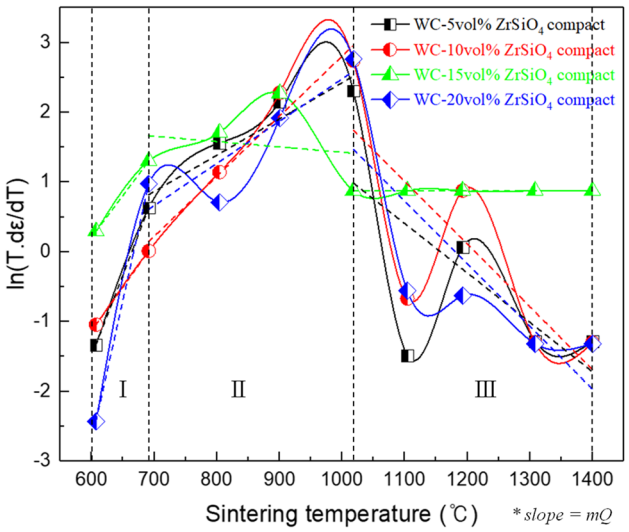


**Fig. 5** Variation of strain rate (dε/dT) and apparent activation energy (Q) from non-isothermal sintering of WC-$ZrSiO_4$ hard materials

evaporation of the molten layer of inter-particles during surface activation, which was caused by the pulse current from spark plasma [32, 33]. In accordance with R. L. Coble's model, in stage II, it was assumed that there were two diffusion pathways for the lattice (m = 0.5) and grain boundary (m = 0.33) [34]. The Q value of the WC-15 vol% $ZrSiO_4$ suggested that the subsequent diffusion [22] from the distorted lattice to the grain boundary could be completed in a lower activation energy range (74.32–111.48 kJ $mol^{-1}$). During stage II, the low activation energy might be more dominant compared to the densification behavior, which was due to a combination of induced particle arrangements that lead to sliding and dislocation of the grain boundaries [22]. Thus, the densification rate was discerned using the variation of the slope (mQ) in terms of activation energy. Stage III had relatively high activation energies, whereas shrinkage was practically saturated and stopped in this stage (Fig. 2). This, phenomenon was related to the elimination of residual isolated porosity and the growth of grains.

Figure 6 illustrates the structural evolution of WC-$ZrSiO_4$ hard materials from powders to compacts, and the lattice parameters of WC in the basal plane are presented in Table 2. The XRD peak shifts showed that the tungsten carbide in the basal plane had a distorted interplanar spacing because of plastic deformation. Notably, the strain softening mechanism owing to larger plastic deformation or plastic strain made it easy to form a neck as well as for further grain growth as part of a grain-boundary-mediated mechanism with grain rotation. However, higher micro-strains (5 vol% zircon had $\epsilon = 0.51$; and 15 vol% zircon, $\epsilon = 0.64$) oriented to the basal planes could cause abnormal grain growth [35, 36].

**Table 1** Variation of apparent activation energy (Q) for WC-$ZrSiO_4$ compacts during SPS process

| Specimen | Apparent activation energy (Q) at the stage I (600–700 °C) kJ/mol | Apparent activation energy (Q) at the stage II (700–1000 °C) kJ/mol | Apparent activation energy (Q) at the stage III (1000–1400 °C) kJ/mol |
|---|---|---|---|
| WC-5 vol% $ZrSiO_4$ compact | 68.37 | 27.44 | 75.58 |
| WC-10 vol% $ZrSiO_4$ compact | 69.91 | 62.61 | 111.42 |
| WC-15 vol% $ZrSiO_4$ compact | 48.86 | 39.16 | 86.72 |
| WC-20 vol% $ZrSiO_4$ compact | 42.84 | 67.93 | 155.74 |

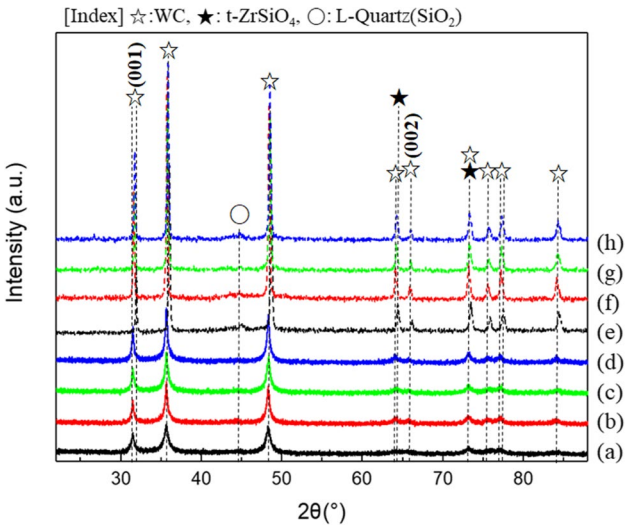


**Fig. 6** XRD patterns of WC-$ZrSiO_4$ hard materials with different volume fraction: **a** WC-5 vol% $ZrSiO_4$ powder, **b** WC-10 vol% $ZrSiO_4$ powder, **c** WC-15 vol% $ZrSiO_4$ powder, **d** WC-20 vol% $ZrSiO_4$ powder, **e** WC-5 vol% $ZrSiO_4$ compact, **f** WC-10 vol% $ZrSiO_4$ compact, **g** WC-15 vol% $ZrSiO_4$ compact, and h) WC-20 vol% $ZrSiO_4$ compact

Conversely, undissociated zircon (Fig. 7 [37]) was observed with no martensitic transformation, that is, transormation from tetragonal zircon (t-$ZrSiO_4$) to monoclinic zirconia (m-$ZrO_2$) did not occur [37, 38]. The t-$ZrSiO_4$ could cause softening owing to a possible brittle to ductile transition caused by the formation of a component within the WC, which could be enough to favor plastic deformation.

Figure 8 shows the microstructural evolution of the WC-$ZrSiO_4$ hard materials. As seen in the XRD patterns, Fig. 8a shows the crowded abnormal grain growth of tungsten carbide at 5 vol% zircon compared to the other hard materials. These coarse-grained materials enhance both fracture toughness and tensile strength [39, 40]. Furthermore, Fig. 8c displays the brittle-brittle component (gray) regions of 15 vol% zircon, which had most the homogeneous distribution in the matrix among the presented WC-$ZrSiO_4$ hard materials. In the other WC-$ZrSiO_4$ consolidation products, according to the zircon content, the zircon-rich-phase could only be observed (Fig. 8d) along with well-defined grain boundaries of tungsten carbide.

**Table 2** Variation of lattice parameter and micro strain from powder to compacts in basal planes of WC-$ZrSiO_4$ hard materials

| Specimen | Phase state | | | | | |
|---|---|---|---|---|---|---|
| | Powder | | | Compact | | |
| | 2θ (°), (plane) | d-spacing (Å) | Micro strain (ε) | 2θ (°), (plane) | d-spacing (Å) | Micro strain (ε) |
| WC-5 vol% $ZrSiO_4$ | 31.481 (001) | 2.841 | 0.366 | 31.899 (001) | 2.805 | 0.210 |
| | 66.054 (002) | 1.415 | 0.605 | 66.166 (002) | 1.412 | 0.153 |
| WC-10 vol% $ZrSiO_4$ | 31.469 (001) | 2.842 | 0.233 | 31.584 (001) | 2.832 | 0.212 |
| | 65.743 (002) | 1.420 | 0.215 | 65.850 (002) | 1.418 | 0.164 |
| WC-15 vol% $ZrSiO_4$ | 31.514 (001) | 2.838 | 0.321 | 31.702 (001) | 2.822 | 0.211 |
| | 65.795 (002) | 1.419 | 0.437 | 65.965 (002) | 1.416 | 0.163 |
| WC-20 vol% $ZrSiO_4$ | 31.491 (001) | 2.840 | 0.232 | 31.710 (001) | 2.821 | 0.253 |
| | 65.735 (002) | 1.420 | 0.215 | 65.992 (002) | 1.415 | 0.163 |

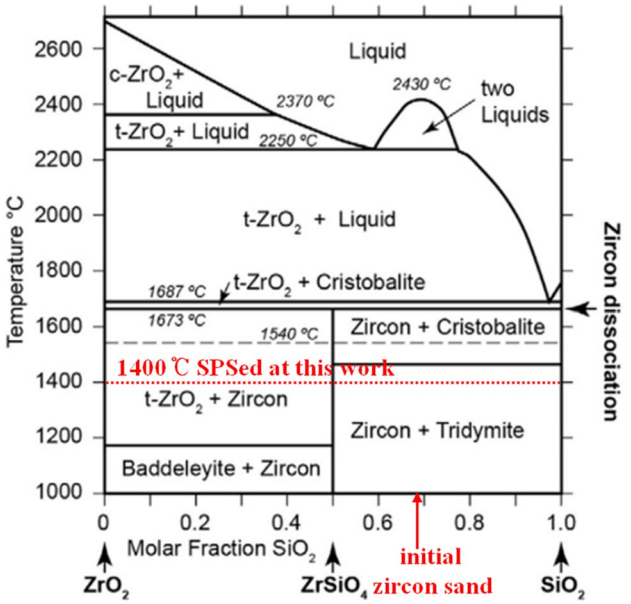


**Fig. 7** Phase diagram for $ZrO_2$-$ZrSiO_4$-$SiO_2$ system modified after Telle et al. [38]

Figure 9 shows the mechanical properties of the WC-$ZrSiO_4$ hard materials. The hardness decreased from $1868.5 \pm 33.1$ to $1643.5 \pm 20.4$ kg mm$^{-2}$, whereas the fracture toughness improved from $10.8 \pm 0.28$ to $12.9 \pm 0.27$ MPa m$^{1/2}$. In particular, the WC-15 vol% $ZrSiO_4$ achieved moderate hardness ($1691.9 \pm 19.4$ kg mm$^{-2}$) and fracture toughness (12.7 MPa m$^{1/2}$ $\pm$ 0.27) owing to the effects of the higher densification rate and the history of plastic deformation ensuring ductility.

Figure 10 demonstrates the propagation of microcracks, and was used to examine the improvement in the fracture toughness of tungsten carbide due to the addition of zircon. The propagation of the microcracks was classified according to several mechanisms that involve bridging, deflection, absorbed, intergranular, and transgranular fractures [41–43]. Crack bridging (*see* indexes 1 and 5) in stretched WC-$ZrSiO_4$ or $ZrSiO_4$ curbed further cracking by preventing the occurrence of preferential microcracks (*see* indexes 2 and 3), thereby toughening the composite [41]. Moreover, the derived crack bridging effect surrounded the precipitated zircon because of the crack deflection of tungsten carbide. This effect was

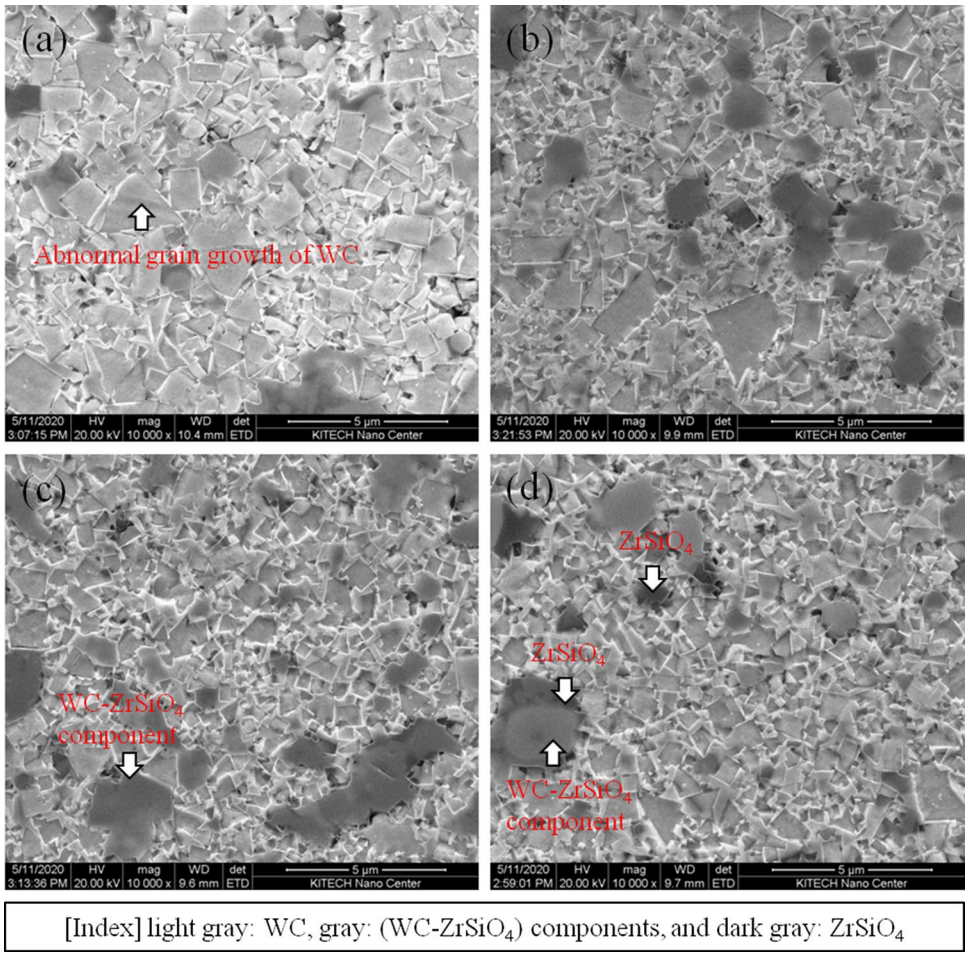


**Fig. 8** FE-SEM images of WC-$ZrSiO_4$ compacts: **a** WC-5 vol% $ZrSiO_4$, **b** WC-10 vol% $ZrSiO_4$, **c** WC-15 vol% $ZrSiO_4$ and **d** WC-20 vol% $ZrSiO_4$

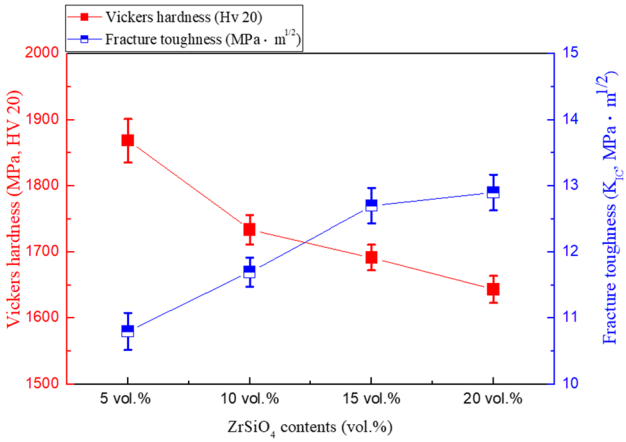


**Fig. 9** Variation of mechanical properties of WC-$ZrSiO_4$ compacts

responsible for the increased fracture toughness, and it could act as an effective mediator in the propagation of transgranular fractures. For instance, two toughening paths can be described by indexing connections, such as 4 → 5 → 6 and 4 → 1 → 5 as shown in Fig. 10b, c, respectively. Consequently, it can be seen that the brittle cracks were absorbed in the zircon-rich areas, and that the propagation of crack bridging (in the WC-$ZrSiO_4$ component) is an effective way to strengthen composites (e.g., 2 → 7 → 8 → 1), as shown in shown Fig. 10d.

## 4 Conclusions

Cemented carbide materials with zircon and improved toughness were produced in a fully densified state via SPS, which was preceded by the mechanical activation of the respective powders. Planetary ball milling was employed to produce brittle-brittle components (WC-$ZrSiO_4$) containing strained products. The brittle-brittle for inter-particle component had a dominant effect on the sintering kinetics and were driving force of densification during SPS proces. The sintering parameters such as macroscopic shrinkage strain, sintering exponent, strain rate, and apparent activation energy were described in relation to the microstructural evolution. The lattice distortion and micro-strain were observed in the basal planes of tungsten carbide as well as the behaviors of plastic deformation and abnormal grain growth induced by toughening due to undissociated tetragonal zircon. The mechanical properties of the WC-$ZrSiO_4$ hard materials were investigated using the trace of an indentation. In particular, the material produced by the addition of 15 vol% $ZrSiO_4$ possessed the desirable moderate hardness and fracture toughness values because of its higher densification rate and homogeneous distribution of zircon. The toughness of WC-$ZrSiO_4$ hard materials was validated by observing the microstructure after crack propagation and the types of cracks that ensued, such as bridging, deflection, absorbed, intergranular, and transgranular fractures.

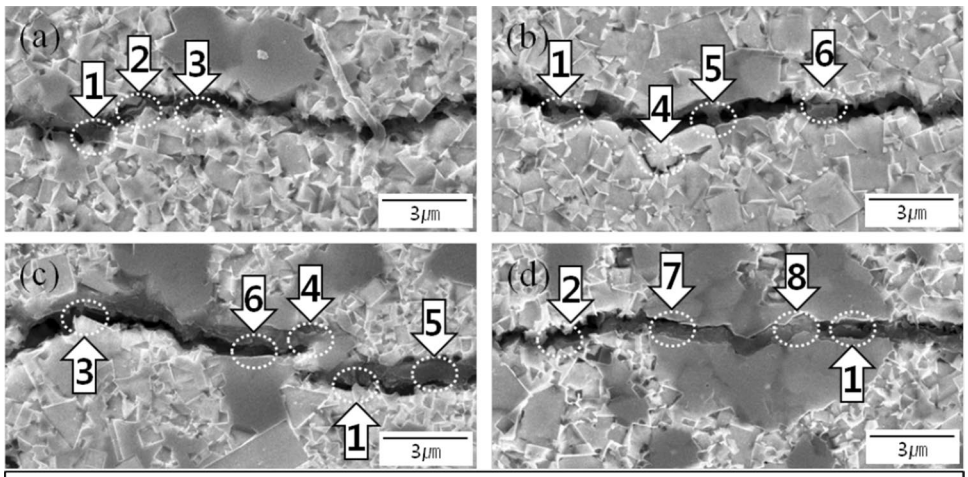


**Fig. 10** Microcrack propagations in WC-$ZrSiO_4$ compacts: **a** WC-5 vol% $ZrSiO_4$, **b** WC 10 vol% $ZrSiO_4$, **c** WC-15 vol% $ZrSiO_4$ and **d** WC-20 vol% $ZrSiO_4$

**Acknowledgements** This study has been conducted with the support of the Korea Institute of Industrial Technology as "Production technology commercialization project (KITECH EO-20-040)".



## 5. References

1. A. Rizzo, S. Goel, M.L. Grilli, R. Iglesias, L. Jaworska, V. Lapkovskis, P. Novak, B.O. Postolnyi, D. Valerini, Materials **13**, 1377 (2020)
2. D. Kurniawan, N.M. Yusof, S. Sharif, Mater. Manuf. Process. **25**, 370 (2010)
3 D. Dong, X. Xiang, B. Huang, H. Xiong, L. Zhang, K. Shi, J. Liao, Vaccum **179**, 109571 (2020)
4 Q. Tang, J. Yang, H. Yang, J. Ruan, Ceram. Int. **42**, 18100 (2016)
5. J.H. Lee, H.K. Park, J.H. Jang, I.H. Oh, Met. Mater. Int. **25**, 268 (2019)
6. Y.A. Alshataif, S. Sivasankaran, F.A. Al-Mufadi, A.S. Alaboodi, H.R. Ammar, Met. Mater. Int. **26**, 1099 (2020)
7. R. Rumman, L.C. Chuan, J.S. Quinton, R. Ghomashchi, Met. Mater. Int. **26**, 844 (2020)
8 J.M. Tarrago, G. Fargas, E. Jimenez-Pique, A. Felip, L. Isern, D. Coureaux, J.J. Roa, I. Al-Dawery, J. Fair, L. Llanes, Powder Metall. **57**, 324 (2014)
9. M. Roosta, H. Baharvandi, Int. J. Refract. Met. H. **37**, 29 (2013)
10. T. Langa, P. Olubambi, T. Shabalala, M.B. Shongwe, Int. J. Refract. Met. H. **72**, 341 (2018)
11. M. Roosta, H. Baharvandi, H. Abdizade, Int. J. Refract. Met. H. **29**, 710 (2011)
12. S.A. Rasaki, B. Zhang, K. Anbalgam, T. Thomas, M. Yang, Prog. Solid State Ch. **50**, 1 (2018)
13 Y. Han, Y. Dai, D. Shu, J. Wang, B. Sun, J. Alloy. Compd. **438**, 327 (2007)
14. H. Abdizadeh, M. Ashuri, P.T. Moghadam, A. Nouribahadory, H.R. Baharvandi, Mater. Design **32**, 4417 (2011)
15. S. Robert Jr., H.J. Pavlik, Holland, J. Am. Ceram. Soc. **84**, 2930 (2001)
16. P.Y. Lee, C.C. Koch, Appl. Phys. Lett. **50**, 1578 (1987)
17. E. Ghasali, H. Nouranian, A. Rahbari, H. Majidian, M. Alizadeh, T. Ebadzadeh, Mater. Res. **19**, 1189 (2016)
18. N.M. Rendtorff, S. Grasso, C. Hu, G. Suarez, E.F. Aglietti, Y. Sakka, Ceram. Int. **28**, 1793 (2012)
19. M.C. Anjali, P. Biswas, D. Chakravarty, U.S. Hareesh, Y.S. Rao, R. Johnson, Sci. Sinter. **44**, 323 (2012)
20. F.B. Swinkels, M.F. Ashby, Acta Metall. **29**, 259 (1981)
21. D. Lahiri, S.V. Ramana Rao, G.V.S. Hemantha Rao, R.K. Srivastava, J. Nucl. Mater. **357**, 88 (2006)
22. A.K. Nanda, K. Kurokawa, in *Tungsten carbide – Processing and applications*, ed. by K. Liu. Spark Plasma Sintering of Ultrafine WC Powders: A Combined Kinetic and Microstructural Study (IntechOpen, London, 2012)
23 A.R. Stokes, A.J.C. Wilson, Proc. Phys. Soc. **56**, 174 (1944)
24. R.D. Dukino, M.V. Swain, J. Am. Ceram. Soc. **75**, 3299 (1992)
25 J.H. Ma, L.C. Lim, J. Eur. Ceram. Soc. **22**, 2197 (2002)
26. R.M. Davis, B. McDermott, C.C. Koch, Metall. Trans. A **19**, 2867 (1988)
27 C. Suryanarayana, Prog. Mater. Sci. **46**, 1 (2001)
28. M.H. Ghasemi, B. Ghasemi, H.R.M. Semnani, Met. Mater. Int. **25**, 1008 (2019)
29. W.Y. Shih, W.H. Shih, I.A. Aksay, J. Mater. Res. **10**, 1000 (1995)
30. M.Q. Zeng, J.L. Tu, M. Zhu, W. Wang, J.W. Liu, Z.C. Lu, Met. Mater. Int. **26**, 1374 (2020)
31. R.M. German, Crit. Rev. Solid State **35**, 236 (2010)
32. S. Nam, S.E. Shin, J.H. Kim, H.J. Choi, Met. Mater. Int. **26**, 1385 (2020)
33. J.M. Montes, F.G. Cuevas, F.J.V. Reina, F. Ternero, R. Astacio, E.S. Caballero, J. Cintas, Met. Mater. Int. **26**, 1045 (2020)
34. R.L. Coble, J. Am. Ceram. Soc. **41**, 55 (1958)
35. B. Chen, L. Zhu, Y. Xin, J. Lei, Quantum Beam Sci. **3**, 17 (2019)
36. L. Wang, J. Teng, P. Liu, A. Hirata, E. Ma, Z. Zhang, M. Chen, X. Han, Nat. Commun. **17**, 4402 (2014)
37 X.J. Jin, Curr. Opin. Solid St. M. **9**, 313 (2005)
38 R. Telle, F. Greffrath, R. Prieler, J. Eur. Ceram. Soc. **35**, 3995 (2015)
39 J. Garcia, V.C. Cipres, A. Blomqvist, B. Kaplan, Int. J. Refract. Met. H. **80**, 40 (2019)
40. K. Shirvanimoghaddam, M.K. Akabari, H. Abdizadeh, A.H. Pakseresht, F. Abdi, A. Shahbazkhan, Kovove Mater. **53**, 139 (2015)
41 G. Pezzotti, H. Huebner, H. Suenobu, O. Sbaizero, T. Nishida, J. Eur. Ceram. Soc. **19**, 119 (1999)
42 J. Watts, G. Hilmas, Int. J. Refract. Met. H. **24**, 222 (2006)
43. P.R. Fry, G.G. Garrett, J. Mater. Sci. **23**, 2325 (1988)